RSC Advances

PAPER

View Article Online
View Journal | View Issue

Cite this: *RSC Adv.*, 2023, **13**, 21190

Enhancement of photoacoustic and upconversion emission in Mg^{2+}/Zn^{2+} codoped Gd_2O_3: Er^{3+}/Yb^{3+} phosphor using 980 nm excitation†

Minarul I. Sarkar, K. V. Cinumon and Kaushal Kumar *

Received 7th May 2023
Accepted 3rd July 2023

DOI: 10.1039/d3ra03041e

rsc.li/rsc-advances

In this work, Er^{3+}/Yb^{3+} doped Gd_2O_3 phosphor samples were synthesized through a combustion method and then characterized through X-ray diffraction and FE-SEM techniques. The sample was studied for photoacoustic spectroscopy (PAS) and upconversion (UC) emission spectroscopy techniques using a frequency modulated 980 nm excitation source. A correlation between PA signal (produced due to non-radiative transitions) and UC emission intensity (produced due to radiative transition) is made in order to optimize the sample for both these properties. The phosphor was codoped with Mg^{2+} and Zn^{2+} ions to see enhancement in upconversion emission intensity and these ions have enhanced the upconversion emission. Studies show that the present phosphor is appropriate for producing strong upconversion emission intensity along with a strong photoacoustic signal which is beneficial for upconversion-imaging as well as photothermal therapy. The present sample has also shown its potential for detection of fingerprints.

1. Introduction

Rare earth doped phosphor materials have been broadly studied for different applications including light emitting diodes (LEDs), solid-state lighting, night glowing panels and emergency signs, high-definition televisions (HD-TVs), latent fingerprint detection, temperature sensing, medical diagnostics, *in vivo* imaging and laser therapy.[1–10] The interest in rare earth doped phosphor materials has augmented due to the exceptional optical properties of rare earth ions.[11–15] The upconversion (UC) luminescence of rare earth ions mostly originates from the electronic transitions within the 4f-shell of the rare earth ions. The rare earth ions possess many electronic energy levels spanning from the UV to NIR region and many of them are metastable in character which supports the UC emission. The high UC intensity from the phosphor could be achieved using lower phonon energy host materials.[16] Out of various phosphor materials, the Er^{3+}/Yb^{3+} doped Gd_2O_3 phosphor material has been considered as highly efficient for high upconversion (UC) emission intensity.[17–21]

Gadolinium oxide (Gd_2O_3) is an ideal host material for preparation of phosphor material due to its low phonon energy (600 cm^{-1} in bulk form).[22] Moreover the luminescence intensity depends on various parameters, such that concentration of each oxide, crystallite size, surface area, morphologies, reactants, and sample preparation method.[23–25] At present, combustion synthesis of phosphors using organic fuels has become attractive because of the advantages (over other conventional methods), *e.g.*, high purity, low processing temperature, homogeneous mixing uniform and spherical particle size. Low energy consumption makes this technique most suitable for large scale production. The phosphor materials have been prepared by follows different synthesis methods such that microwave, sol–gel, co-precipitation, hydrothermal, combustion *etc.*[26–30] Among all these reported methods, combustion is better one as the produced sample by this methods are highly homogeneity, low cost, and less synthesis time.

The efficiency luminescence properties of rare-earth doped phosphor materials are of great importance to broaden their applications, particularly in the application of biomedical field.[31] The UC intensity of rare-earth doped phosphor materials depends on the probability of intra-4f electronic transition and that significantly affected by the crystal symmetry nearby rare-earth ions.[32] Many researchers have reported the effect of non-rare-earth ions of Fe^{3+}, Sc^{3+}, Bi^{3+}, Cd^{2+}, Zn^{2+}, Mg^{2+}, Mn^{2+}, Li^{+}, K^{+} *etc.* on different phosphor material for efficiency of UC intensity.[31–39] All these mention researchers have demonstrated that in presence of alkali metal or non-rare-earth dopant ions into the host lattice is a better methodology to attain high luminescence intensity. In this work, the authors have synthesized Gd_2O_3: Er^{3+}/Yb^{3+} phosphors and co-doped with 8 mol% of Mg^{2+} and Zn^{2+} ions and showed that for Zn^{2+} doped phosphor material has more UC efficiency compared to Mg^{2+}.[40]

Optical Materials & Bio-Imaging Research Laboratory, Department of Physics, Indian Institute of Technology (Indian School of Mines) Dhanbad, Dhanbad 826004, India. E-mail: kkumar@iitism.ac.in

† Electronic supplementary information (ESI) available. See DOI: https://doi.org/10.1039/d3ra03041e

In the present work Gd_2O_3: Er^{3+}/Yb^{3+} phosphors were synthesized by combustion method and for enhancement of UC emission intensity the divalent Mg^{2+} and Zn^{2+} ions were added into the optimized rare earth ions concentration. The crystal phase was confirmed by XRD and surface morphology were studied by FE-SEM technique. The UC and PA spectra of the final sample (Gd_2O_3: $0.3Er^{3+} + 2.0Yb^{3+} + 8.0Zn^{2+}$) were recorded by varying pump power and a comparative study is made between UC intensity (radiative transitions) and PA signal amplitudes (non-radiative transitions).

2. Materials and methods

2.1 Chemicals used for sample synthesis

For synthesis of the phosphor, gadolinium oxide (Gd_2O_3, 99.99% pure, Sigma Aldrich), erbium oxide (Er_2O_3, 99.99% pure, Sigma Aldrich), ytterbium oxide (Yb_2O_3, 99.99% pure, Sigma Aldrich), urea (CH_4N_2O, 99.99% pure, Alfa Asear) and nitric acid (HNO_3, 90.0% pure, Finar Chemicals, India) were used as precursors agent. Triply distilled DI water was used throughout the synthesis reaction.

2.2 Sample synthesis and characterization

Gd_2O_3: Er^{3+}/Yb^{3+} phosphors were synthesized by followed combustion synthesis method.[41] The chemical compositions of starting materials were taken followed by proportions equations given below:

$$(100 - x - y)Gd_2O_3 + xEr_2O_3 + yYb_2O_3;\ \text{where, } x = 0.1\text{–}0.4\ \text{mol\% and } y = 1.0\text{–}2.5\ \text{mol\%}.$$

$$(100 - 0.3 - 2.0 - z)Gd_2O_3 + 0.3Er_2O_3 + 2.0Yb_2O_3 + zMgO;\ \text{where, } z = 8\ \text{mol\%}.$$

$$(100 - 0.3 - 2.0 - z')Gd_2O_3 + 0.3Er_2O_3 + 2.0Yb_2O_3 + z'ZnO;\ \text{where, } z' = 8\ \text{mol\%}.$$

Firstly, for preparation of nitrates of oxides, appropriate amount of each oxide was taken in separate glass beakers (20 mL) and excess amount of nitric acid was added into them. Then the beaker was placed on hot-plate of the stirrer maintain temperature at 90 °C and the rotation frequency of the magnetic bead was fixed at 350 rpm until it forms transparent solution. After attaining of transparent solutions extra nitrate was vaporized by adding DI-water. Then all evaporated nitrates of all oxides were collected in a single beaker (100 mL) and mixed them for another 30 minutes. On the other hand, 10 mL DI water was taken in a separate beaker (20 mL) and specific amount of urea was added. Then the temperature of the bath was raised to 100 °C until gel was formed. Then the obtained gel was shifted into alumina–crucible for combustion reaction. Then the crucible was placed into a preheated muffle furnace of temperature around at 600 °C. After placing the crucible into furnace, gel melts and within few minutes it catches fire. After completion of the burning, large foamy form of material was found. The obtained material was crushed with the help of the mortar pastel to acquire fine powder. The obtained sample was used for heat treatment at temperatures of 800, 1200 and 1400 ° C for 4 h for improvement of UC properties. Also, two phosphor samples were synthesized followed by same experimental conditions with addition of specific amount (8 mol%) of MgO and ZnO. Finally, the samples were stored in a desiccator at room temperature.

The X-ray diffraction (XRD) patterns were recorded by diffractometer X-ray panalytical X'pert pro (model: Rigaku TTRX-III, Japan) in between 2θ range of 10–80°. The morphological images were recorded by FE-SEM by Supra 55 (Carl Zeiss, Germany) and the particle size was measured by ImageJ software. For FE-SEM and EDAX measurements the powder sample was attached on the sample holder with the help of carbon tape. As the samples were non-conducting, first the sample surface was coated with gold using a low-temperature induction-based sample coating system. Then the samples were kept in the sample chamber under high vacuum. The UC emission intensity of the samples was recorded by CCD-based spectrometer (model: ULS2048x58, Avantes, USA). The electronic absorption spectra were recorded by UV-VIS-NIR spectrophotometer (model: Cary 5000, Agilent, USA). The PA spectrum of the samples was measured by home assembled PA spectrometer containing of an immense optical spectrograph.

2.3 Photoacoustic spectroscopy of samples

In PA spectroscopy, periodic chopped light beam interacts with molecules or atoms of the sample inside the cell chamber and is promoted to higher energy state (excited state). Molecules or atoms in higher level come back to lower energy levels (ground state) by two natural ways. One way is by emission of photon (radiative process) and which is studied by recording UC emission spectroscopy. Another way is emission of phonon (non-radiative process) and which is studied by recording the PA spectrum. In the non-radiative process, heat is produced due to phonons. As chopped optical light or pulse laser is incident into the sample, the heat produced is periodic and produces periodic heat. This periodic heat produces small air fluctuations which are detected through sensitive microphone.

2.4 Experimental setup for UC and PA measurement

In the present work, the experimental setup is designed for a comparative study of power-dependent UC emission and PA amplitude measurement. The PA cell is the most important part of spectroscopy. For maximum sensitivity of the system, the PA cell was designed followed by the R-G model.[42] In our previous work, the fabrication of a sensitive PA cell was discussed in detail.[43,44] The schematic diagram of the PA cell and the homemade cell in laboratory are given Fig. S1 (ESI†). The power-dependent PA amplitudes and UC emission were recorded by using the experimental setup presented in Fig. 1. From the left, power-adjustable continuous 980 nm diode laser (model: PSU-H-LED, C.N.I. Optoelectronics tech. Co. Ltd, China) was used for sample excitation. For the production of PA signals inside the cell, a periodic heat supply is required. For this, a mechanical chopper (model: SR 540, Stanford Research Systems, INC)

was placed in front of the laser output, and the frequency of the chopper was adjusted by the knob in the chopper source. Some optical lenses and mirrors were used for proper alignment so maximum light entered into the cell chamber and incident on the sample with extreme intensity. For detection of the noise, a pre-polarized microphone (model: 4966, Brüel & Kjær, Germany) of sensitivity 50 mV Pa^{-1} was fitted with the cell wall and it was connected with a chamber through 1 mm thick channel. Then, a gain adjustable commercial pre-amplifier (model: 1704, Bruel & Kjaer, Germany) was connected before being fed to the lock-in-amplifier for amplification of the weak electrical signal produced by the microphone. For store PA data a lock-in-amplifier (model: SR-830, Stanford Research System, USA) was used as a data acquisition device. The experimental setup presented in Fig. S2 (ESI†) was used for recording PA absorption spectra of the sample. The instrumental setup was the same as mentioned in the previous one, only the optical laser source was replaced by a large spectrograph (model: 9055F, Sciencetech, Canada) assembled with 500 watt. xenon lamp. The spectrograph has a focal length of 250 mm and a grating size of 64 × 64 mm. Big grating size promises high light collection and projection (f-number = f/2.5). Furthermore, the xenon lamp was attached on-axis with an elliptical reflector at the entrance slit of the spectrograph. All data of PA amplitudes and UC intensity were recorded at room temperature 22 °C and the temperature was measured by a digital thermometer.

3. Results and discussion

3.1 X-ray diffraction analysis

X-ray diffraction data (XRD) was recorded for confirmation of the crystal phase of synthesized phosphor samples. The XRD pattern of the samples annealed in 800–1200 °C range for 4 h are shown in Fig. 2. Among all, the most intense peaks are observed near 2θ values at 26.16, 28.8, 30.01, 30.65, 31.69, 32.32, 33.04, 38.89, 42.99, 48.04, 51.14, 53.84, and 55.62 corresponding to (hkl) plane (202) (111), (401), (402), (003), (310), ($\bar{1}$12), (600), ($\bar{3}$13), (313), (020), ($\bar{7}$12), and (022) respectively. The sample has some amorphous nature heated in low temperature but the crystallinity improved at higher annealed temperature. The crystallite size was measured by using 'Scherer equation' mention in eqn (1);

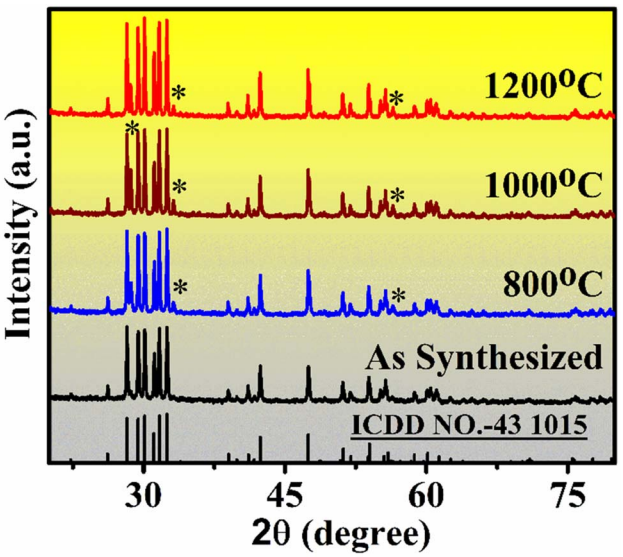

Fig. 2 XRD pattern of Er^{3+}/Yb^{3+} doped Gd_2O_3 phosphor powder samples annealed at different temperatures (800–1200 °C) for 4 h.

$$d = \frac{\lambda \times 0.9}{\beta \times \cos\theta} \quad (1)$$

where d is the crystallite size of the sample for (hkl) plane, λ is the wavelength of the X-ray radiation, β is the full width at half maxima (FWHM) in radian, and θ is the diffraction angle at the same (hkl) plane. The average value of crystallite size corresponding to seven intense diffraction peaks is found 15.6 nm. Also, the crystallite size increased with annealed temperature and measured 28.2, 43.7, and 55.6 nm for 800, 1000, and 1200 °

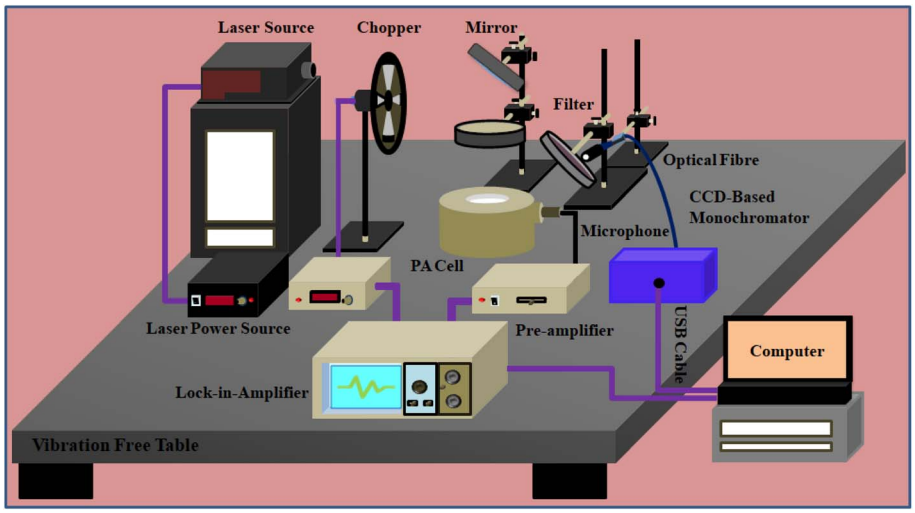

Fig. 1 Full experimental setup for recording of power dependent UC spectra and PA amplitudes simultaneously.

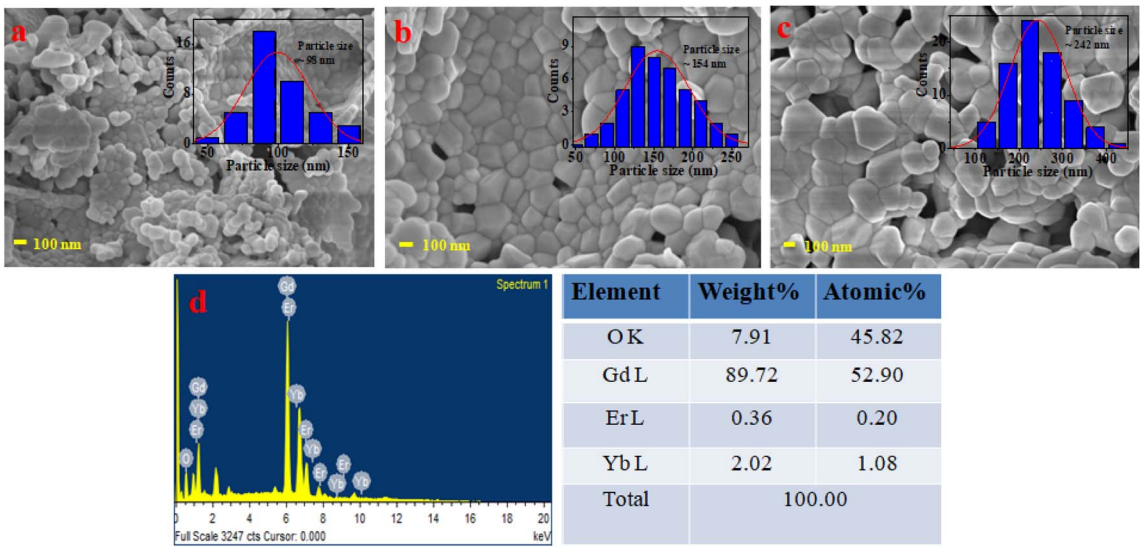

Element	Weight%	Atomic%
O K	7.91	45.82
Gd L	89.72	52.90
Er L	0.36	0.20
Yb L	2.02	1.08
Total	100.00	

Fig. 3 FE-SEM images for $0.3Er^{3+}$ + $2.0Yb^{3+}$: Gd_2O_3 phosphor sample annealed at different temperatures for 4 h. (a) Annealed at 800 °C, (b) 1000 °C, (c) 1200 °C, (d) EDAX spectrum with % of elemental compositions.

C, respectively. In higher annealed temperatures, some extra peaks are observed (* marked in Fig. 2) near 28.61, 33.17, and 56.53 corresponding to (022), (400), and (622). This pattern is very close to the ICDD file no 43-1014 and that result showed the cubic crystalline phase of the phosphor.[41]

3.2 FE-SEM and EDAX analysis

The morphological structures of all samples were analyzed by FE-SEM. The powder sample was attached on the sample holder by carbon tapes for recording FE-SEM and EDAX spectrum. As the samples were non-conducting, first the samples were coated with gold using a low-temperature induction-based sample coating system. Then the samples were kept in the sample chamber and made the chamber highly vacuumed for recording FE-SEM images and EDAX spectrum. All data for both FE-SEM and EDAX were recorded at 20 °C of fixed room temperature. The FE-SEM images are recorded at the same magnification of 100 nm. The FE-SEM images for the sample annealed at temperatures 800, 1000, and 1200 °C are shown in Fig. 3(a)–(c), respectively. In the images clearly shown that the particle sizes are improved in higher annealed temperatures. The particle size of all samples is measured by ImageJ software and particle size distribution is inserted into FE-SEM images. The average particle size of the sample annealed for 800 °C was measured 98 nm and for 1000 °C & 1200 °C the particle sizes were 154, and 242 nm respectively.

The elemental composition of the optimized sample was analyzed by EDAX. The EDAX spectrum is shown in Fig. 3(d) and the elemental composition is presented in table form on the side of EDAX spectrum. The extra elements carbon (C) and gold

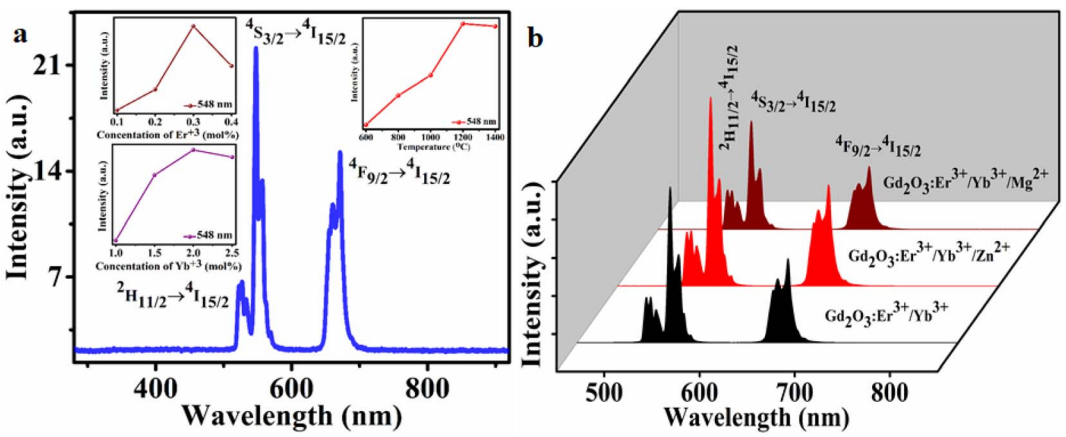

Fig. 4 (a) Whole recorded UC emission spectrum in 280–920 nm range, inset up (left) shows the emission intensity of the band $^4S_{3/2} \rightarrow {}^4I_{15/2}$ at 548 nm with the concentration of Er^{3+} ions, inset (down) shows the intensity with the concentration of Yb^{3+} ions, and inset up (right) shows the intensity with annealed temperature, (b) the UC intensity for without tri-depend and with tri-doped atom (8 mol%) of Zn^{2+} and Mg^{2+} respectively. For UC measurement excitation source: 980 nm NIR-laser.

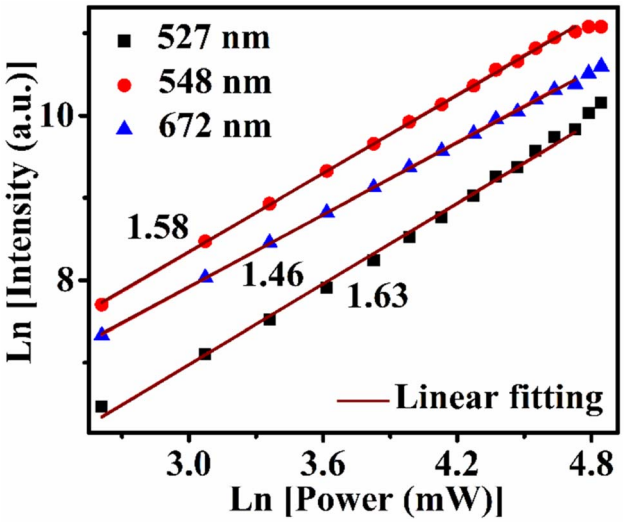

Fig. 5 LnP–LnI plots for number of photon measurement for 527 nm, 548 nm and 672 nm emission bands of Gd_2O_3: $0.3Er^{3+}$ + $2.0Yb^{3+}$ + $8.0Zn^{2+}$ sample.

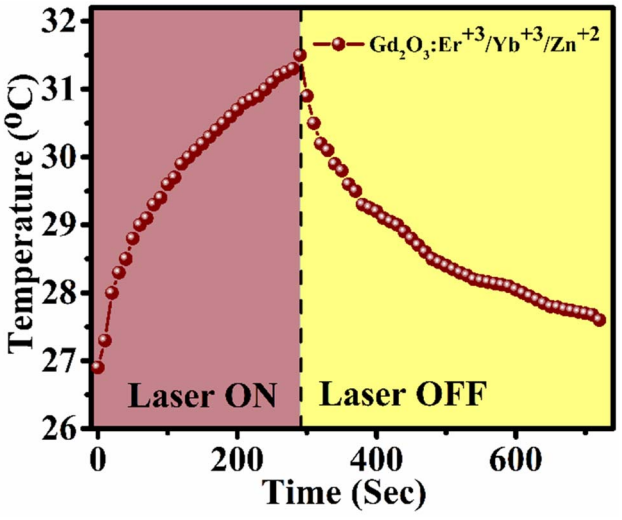

Fig. 6 Temperature profile of Gd_2O_3: $0.3Er^{3+}$ + $2.0Yb^{3+}$ + $8.0Zn^{2+}$ phosphor dispersion (20 mM) in water medium at excitation power of 616 mW and cuvette sample volume of 4 mL.

(Au) were removed from the elemental compositions of the samples.

3.3 Upconversion study

The phosphor sample was optimized for maximum UC intensity by varying concentrations of each doped and sensitizer atom for sample preparation. Firstly, the concentration of Er^{3+} varies (0.1–0.4 mol%) keeping fixed the concentration of Yb^{3+} and for 0.3 mol% measured maximum intensity value. Then the concentration of Yb^{3+} varies (1.0–2.5 mol%) keeping fixed 0.3 mol% concentration of Er^{3+} and measured maximum intensity for 2.0 mol% of Yb^{3+}. Finally, the optimum sample was annealed with varying annealing temperatures of 600–1400 °C for 4 h, and the maximum UC intensity was observed around 1200 °C. The optimization data for the concentration of each doped and annealed temperature are shown inset of Fig. 4(a).

In Fig. 4(b) showed the effect of tri-doped ions (Mg^{2+} & Zn^{2+}) on UC intensity. For the inclusion of the tri-doped ion, the intensity increased with higher rate and enhanced to maximum. In the plot, for 8 mol% of Zn^{2+} measured maximum intensity, and for the same concentration of Mg^{2+} measured less intensity compared to Zn^{2+}. This tri-doped ion also affects the lattice vibration or to the phonon decay discuss below by measuring the PA measurement. The addition of Mg^{2+} ions can result in the destruction of the number of single (non-compensated) cation and oxygen vacancies because of the formation of their associate with Mg^{2+} ion. In fact, the compensation of the extra charge of the single vacancies can significantly diminish the efficiency of trapping of charge carriers.[45] Also, in low concentration of Mg^{2+}, the emission intensity increases but in higher concentration the UC intensity has seen to be quenched due to the formation of excess defect centers in the phosphor lattice.[46]

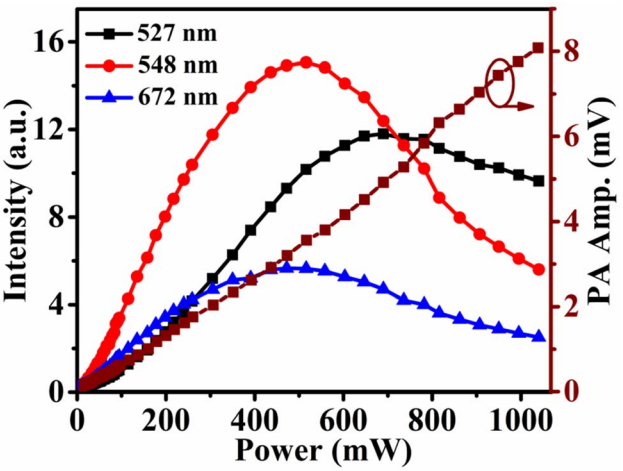

Fig. 7 Data records for comparative study of UC intensity (left scale) and PA amplitudes (right scale) varying excitation power.

Table 1 Calculated values of number photons for different bands by 980 excitation

Excitation power P (mW)	Measured 'n' values for different bands		
	527 nm ($^2H_{11/2} \rightarrow {}^4I_{15/2}$)	548 nm ($^4S_{3/2} \rightarrow {}^4I_{15/2}$)	672 nm ($^4F_{9/2} \rightarrow {}^4I_{15/2}$)
13.6–113	1.63	1.58	1.46

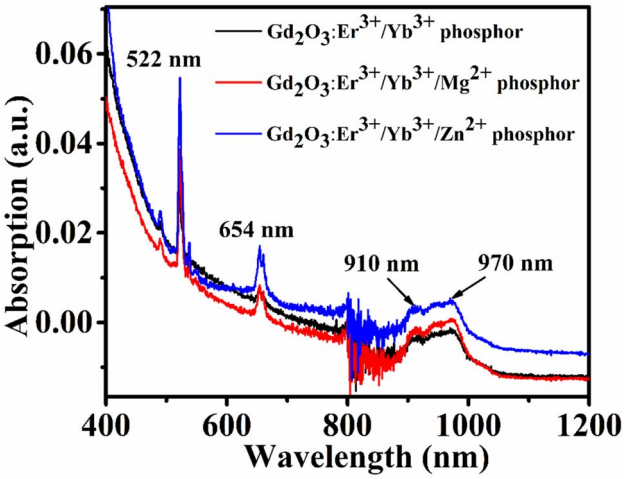

Fig. 8 UV-vis absorption spectra of $0.3Er^{3+}$ + $2.0Yb^{3+}$ (black color), $0.3Er^{3+}$ + $2.0Yb^{3+}$ + $8.0Mg^{2+}$ (red color), and $0.3Er^{3+}$ + $2.0Yb^{3+}$ + $8.0Zn^{2+}$ (blue color) doped Gd_2O_3 phosphor sample annealed at 1200 °C for 4 h.

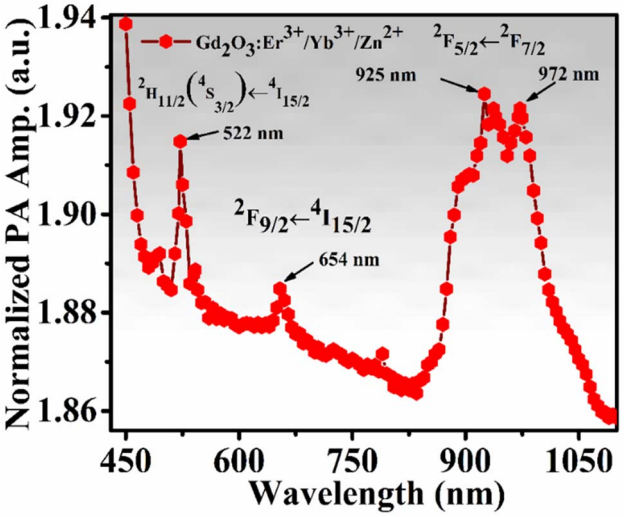

Fig. 9 PA absorption spectrum for phosphor sample annealed at 1200 °C for 4 h.

In the recorded UC emission spectrum showed emission bands around at 527, 548 nm, and 672 nm due to the $^2H_{11/2} \rightarrow {}^4I_{15/2}$, $^4S_{3/2} \rightarrow {}^4I_{15/2}$ and $^4F_{9/2} \rightarrow {}^4I_{15/2}$ transitions, respectively.[9,41,47–49] In the spectrum, maximum intensity measured for the band 548 nm (523 nm) situated in green region and another low intense peak observed near at the red region (672 nm). The schematic energy level diagram of UC mechanism is provided in Fig. S3 (ESI†). The number of photon '*n*' involved in the UC intensity and '*n*' can be measured from the pump power plot LnP *vs.* LnI presented in Fig. 5. The number of incident photons relate with pump power P_{pump} (mW) and emission intensity $I_{UC}(a.u.)$ as;

$$I_{UC}(a.u.) \propto [P_{pump}(\mathrm{mW})]^n \quad (2)$$

The measured values of '*n*' for different bands for the excitation pump power 13.6–113 mW range are shown in Table 1.

3.4 Photothermal conversion efficiency in water medium

The prepared sample was tested for heat generation in water dispersion. For this experiment a 20 mM dispersion of phosphor was prepared in water medium and then heat generation in this sample was compared with pure water on 980 nm excitation. The term photothermal conversion efficiency 'η' specifies that the amount of heat converted from absorbed radiation by the sample. The equation associated to photothermal conversion efficiency is given below in eqn (3).[50,51]

$$\eta = \frac{C_P\left\{\left(\frac{T_{max} - T_\infty}{\tau_P}\right) - \left(\frac{T_{max,0} - T_{\infty,0}}{\tau_{P,0}}\right)\right\}}{P\left(1 - 10^{-A_\lambda}\right)} \quad (3)$$

where P (in mW) is the laser power, A_λ is the absorbance (0.92) of the phosphor dispersion, C_P is the specific heat of water, T_{max} and T_∞ are the maximum achieved temperature by 980 nm laser irradiation into the phosphor dispersion, and surrounding temperature, respectively. The τ_P is the heat dissipated by the cuvette. The $T_{\infty,0}$, $T_{max,0}$, and $\tau_{P,0}$ are the surrounding temperature, maximum temperature achieved for cuvette water system by 980 nm radiation and the time constant for the temperature rise of the cuvette water system, respectively. It is assumed that at low concentration (20 mM) of phosphor dispersion in water medium, the heat capacity C_p is equal to water dispersion medium.

The photothermal conversion efficiency of Gd_2O_3: $0.3Er^{3+}$ + $2.0Yb^{3+}$ + $8.0Zn^{2+}$ (20 mM concentration) in water medium is found to 24.74%. In calculation of this efficiency the thermal effect due to water medium is subtracted as per the above formula. This value indicates that when phosphor particles are dispersed into the water medium the photothermal effect increases. The efficiency could be enhanced further by increasing the phosphor concentration. The temperature profile plot for conversion to heat by 980 nm radiation ($P = 616$ mW) is shown in Fig. 6.

3.5 Comparative studies of PA and UC with excitation power

The data for comparative studies of upconversion intensity and photoacoustic amplitudes were recorded by the instrumental setup shown in Fig. 1 for the final sample with the highest emission intensity. The comparison data is shown in Fig. 7. Here the most intense peaks at 527, 548, and 672 nm due to the transition bands $^2H_{11/2} \rightarrow {}^4I_{15/2}$, $^4S_{3/2} \rightarrow {}^4I_{15/2}$, and $^4F_{9/2} \rightarrow {}^4I_{15/2}$ respectively are plotted with pump power and simultaneous changes of PA amplitudes variations are plotted on the right scale. The data were recorded for the pump power range 2.24–1040 mW. For a detailed discussion, the power scale (*X*-axis) is divided into subsections. For low pump power 2.24–96 mW, the emission intensity increased with a low rate and the PA signal also varied with the same as the heat generation into the sample due to the non-radiative effect was less valuable. In the next pump power, range 96–260 mW the rate of variations of UC

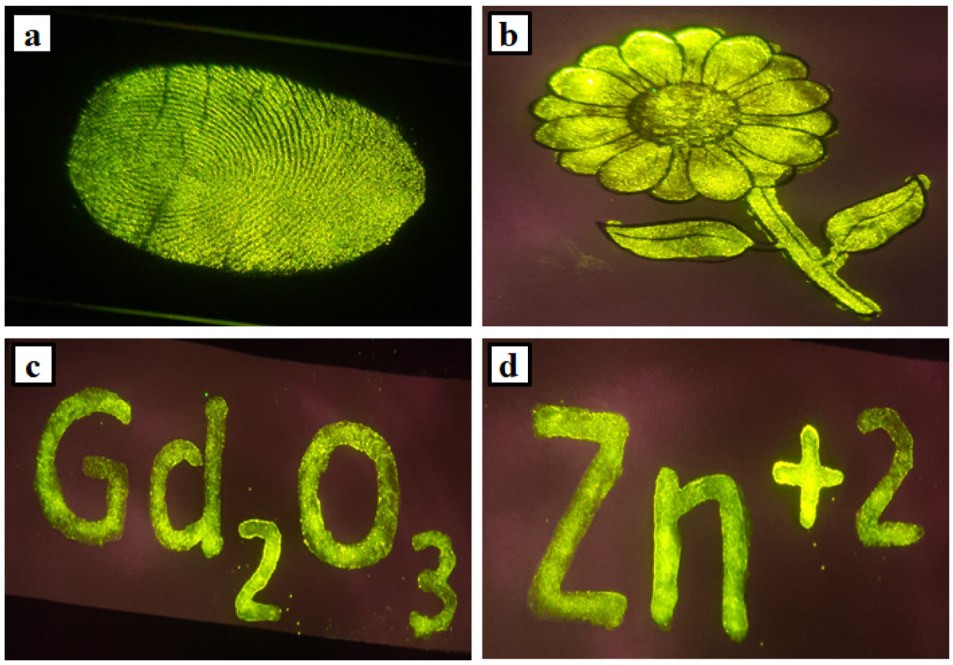

Fig. 10 (a) Fingerprint detection on a glass plate by $0.3Er^{3+}$ + $2.0Yb^{3+}$ + $8.0Zn^{2+}$ (green color) doped Gd_2O_3 phosphor sample annealed at around 1200 °C for 4 h, deposit, and illumination by 980 nm diode laser, (b)–(d) demonstration of security ink for anti-counterfeiting applications by same sample and same illumination condition on plane white paper.

intensity reached maximum value but the PA amplitudes varied with less rate compared to the previous section. In this section the number of photons for UC intensity will increase, so the numbers of phonons for PA signal decreases. In the next section 260–516 mW, the rate of variations of UC intensity will be decreased with a small value and gets saturated. On the other hand, the PA amplitudes variation rate increased with a small value. But in the next section for the 516–1040 mW pump power range, the UC intensity thoroughly decreased for the heating effect of the sample. But the PA amplitudes were varied in the high pump power range and increased simultaneously at a greater rate. So this sample measured the reverse natures of UC intensity (decay of photon) and PA amplitudes variations (decay of phonon) with pump power. The supporting data is given in Table S1 (ESI†). Data shown in Fig. 7 is for extended excitation power range that covers excitation below 13 mW and well above 113 mW power. It was plotted to see the pattern of photo-acoustic signal from low to high excitation power range. Moreover, *Y*-scale values in Fig. 7 are lower than the Fig. 5 as latter measurement was done inside the photo-acoustic cell and beam was chopped using a mechanical chopper. The effective power inside the photo-acoustic cell would be lower due to finite losses due to cell window and chopper blade. Hence intensity recorded in Fig. 7 is lower than Fig. 5.

3.6 UV-vis absorption spectra

The electronic absorption spectra were recorded in 400–1200 nm wavelength range of all three optimum samples is shown in Fig. 8. In the plot clearly shows that the absorption of the samples varied in presence of tri-doped ions. The results showed that after doped of Zn^{2+} ion into the optimum Er^{3+}/Yb^{3+}: Gd_2O_3 phosphor, the absorption increased. On the other hand, the absorption decreased in presence of the dopant ion Mg^{2+}. In the spectrum, two sharp peaks are found around at 522, 654 nm, and another broad peak is observed around 950 nm (938–974 nm range). The first two sharp peaks are allotted for the absorption bands $^2H_{11/2}(^4S_{3/2}) \leftarrow {}^4I_{15/2}$, $^4F_{9/2} \leftarrow {}^4I_{15/2}$ absorption transitions of Er^{3+} ions, and the third broad peak in the 936–974 nm range can be assigned to the $^2F_{5/2} \leftarrow {}^2F_{7/2}$ transition of Yb^{3+} ion.[52]

3.7 PA absorption spectrum

The PA absorption spectrum of the phosphor ($0.3Er^{3+}$ + $2.0Yb^{3+}$ + $8.0Zn^{2+}$-Gd_2O_3) sample was recorded by excited using 500 watts. Xenon lamp. For this measurement, the PA amplitudes for the sample were recorded in varying wavelengths 400–1100 nm range by a software-controlled spectrograph designed by Science Tech Inc., Canada. Then the recorded signals are normalized by the signal recorded by carbon black. The normalized PA absorption spectrum is shown in Fig. 9 and the pattern is very close to the electronic UV-vis absorption spectra.[52] The PA intense peaks are found at 522, and 654 nm for Er^{3+} ion, and one broad peak is observed at 950 nm (938–974 nm range) for sensitizer ion Yb^{3+}.

3.8 Fingerprint detection and security ink application

The Gd_2O_3: Er^{3+}/Yb^{3+}: phosphors have high UC emission intensity and with the addition of divalent Zn^{2+} ions get enhanced. For this efficient intensity, it could positively be used for different applications like fingerprints detections, security

ink for anti-counterfeiting applications *etc.* previously discussed that two intense peaks (527, 548 nm) are situated in the green region and another low intense peak is observed at red region (672 nm). So the overall emission was observed green color from the sample. To progress any crime investigation, fingerprints detections is the first step. In this work, fingerprints are collected from different objects like metal weapons, floors, glasses, windows, doors, or other resources from the crime area and match with the suspect persons. But there were challenges to accumulate fingerprints from such things because of the rough nature of some of the things. So to solve this difficulty, the use of phosphor which has high UC intensity is an impressive idea for fingerprint detection.[41,51] The Gd_2O_3: Er^{3+}/Yb^{3+}/Zn^{2+} phosphor powder is an excellent choice for the recognition of the high-quality fingerprint from any object. Firstly, objects are collected and the surfaces are chosen very carefully. But there the fingerprints are invisible. Now the powder of the phosphor sample has been spread on the surfaces and captures the pictures by illumination with a 980 nm diode laser with sufficient pump power. Then found an apparent vision of fingerprints on the surfaces of the objects. The demonstration of the fingerprint on the plane glass plate is shown in Fig. 10(a).

Then, the final ($0.3Er^{3+} + 2.0Yb^{3+} + 8.0Zn^{2+}$: Gd_2O_3) phosphor sample was used to prepare ink for anti-counterfeiting applications. Around 12 mg of the powder sample was mixed with 8 mL DI water and sonicated for 30 minutes to get a homogeneous mixture of solution. Then using a thin brush fill this ink into a printed flower. Also, using this prepared ink written the words 'Gd_2O_3' and 'Zn^{+2}' on white plane paper. But all are invisible on the paper. Then the pictures were captured through an HD camera during the illumination of each with a 980 nm laser. The recorded clear pictures are shown in Fig. 10(b)–(d).

4. Conclusions

In this work, authors have efficiently fabricated a photoacoustic cell and optimized it for the measurement of photoacoustic spectra of Gd_2O_3: Er^{3+}/Yb^{3+} phosphor. The phosphor sample was synthesized by combustion method and then annealed around 800–1300 °C for 4 h. Samples have shown emission peaks at 527, 548, and 672 nm due to the $^2H_{11/2} \rightarrow {}^4I_{15/2}$, $^4S_{3/2} \rightarrow {}^4I_{15/2}$ and $^4F_{9/2} \rightarrow {}^4I_{15/2}$ transitions, correspondingly. The UC emission is enhanced by codoping of Mg^{2+}/Zn^{2+} ions. The sample showing maximum upconversion emission has also shown maximum photoacoustic signal. The emission studies recommends that the sample is suitable for upconversion imaging and also for photothermal therapy.

Conflicts of interest

The authors have declared that no conflicting interests exist.

Acknowledgements

Authors genuinely thank to the Department of Science and Technology (DST), New Delhi for financial support. Minarul (17DR000415) also thanks to IIT(ISM), Dhanbad for providing research fellowship in terms SRF. One of the authors, Minarul is grateful to the Workshop of IIT(ISM) for their kind help and assistance for cell fabrications.

References

1 M. Pollnau, D. R. Gamelin, S. R. Lüthi, H. U. Güdel and M. P. Hehlen, *Phys. Rev. B: Condens. Matter Mater. Phys.*, 2000, **61**, 3337–3346.
2 M. Zhang, J. Wang, W. Ding, Q. Zhang and Q. Su, *Appl. Phys. B*, 2007, **86**, 647–651.
3 T. R. Hinklin, S. C. Rand and R. M. Laine, *Adv. Mater.*, 2008, **20**, 1270–1273.
4 S. K. Singh, K. Kumar and S. B. Rai, *Sens. Actuators, A*, 2009, **149**, 16–20.
5 V. K. Rai, *Appl. Phys. B*, 2007, **88**, 297–303.
6 C. Feldmann, T. Jüstel, C. r. Ronda and P. j. Schmidt, *Adv. Funct. Mater.*, 2003, **13**, 511–516.
7 C. R. Ronda, *J. Lumin.*, 1997, **72–74**, 49–54.
8 L. Liu, S. K. Gill, Y. Gao, L. J. Hope-Weeks and K. H. Cheng, *Forensic Sci. Int.*, 2008, **176**, 163–172.
9 Z. Li, Q. Han, T. Yan, Z. Huang, Y. Song, Y. Wang and X. Zhang, *J. Alloys Compd.*, 2022, **904**, 164009.
10 D. K. Chatterjee, A. J. Rufaihah and Y. Zhang, *Biomaterials*, 2008, **29**, 937–943.
11 F. Hu, S. Ren, Y. Wu, C. Sun, B. Zhu, Q. Wang, S. Li and D. Zhang, *Spectrochim. Acta, Part A*, 2023, **288**, 122127.
12 M. Chen, Y. Chen, W. Li, C. Yuan, Z. Jia, W. Han and X. Zhang, *J. Alloys Compd.*, 2022, **891**, 161842.
13 L. Wu, P. Dai and D. Wen, *ACS Sustainable Chem. Eng.*, 2022, **10**, 3757–3765.
14 Q. Liu, M. Wu, B. Chen, X. Huang, M. Liu, Y. Liu, K. Su, X. Min, R. Mi and Z. Huang, *Ceram. Int.*, 2023, **49**, 4971–4978.
15 N. Rakov, F. Matias and G. S. Maciel, *Phys. B*, 2023, **652**, 414625.
16 S. I. Klink, G. A. Hebbink, L. Grave, F. C. J. M. Van Veggel, D. N. Reinhoudt, L. H. Slooff, A. Polman and J. W. Hofstraat, *J. Appl. Phys.*, 1999, **86**, 1181–1185.
17 Y. Zhang, H. Jia, X. He, Y. Zheng, R. Bai and H. Liu, *J. Lumin.*, 2021, **236**, 118111.
18 P. Kumar Yadaw, R. K. Padhi, V. Dubey, M. C. Rao and N. Kumar Swamy, *Inorg. Chem. Commun.*, 2022, **143**, 109736.
19 W. Zheng, B. Sun, Y. Li and R. Wang, *ACS Appl. Nano Mater.*, 2021, **4**, 3922–3931.
20 S. Singh, Kanika, G. Kedawat, J. H. Park, B. Ghorai, U. K. Ghorai, C. Upadhyay, B. A. Kaipparettu and B. K. Gupta, *J. Photochem. Photobiol.*, 2021, **8**, 100081.
21 I. Kamińska, A. Wosztyl, P. Kowalik, B. Sikora, T. Wojciechowski, K. Sobczak, R. Minikayev, K. Zajdel, M. Chojnacki, W. Zaleszczyk, K. Łysiak, W. Paszkowicz, J. Szczytko, M. Frontczak-Baniewicz, W. Stryczniewicz and K. Fronc, *Nanotechnology*, 2021, **32**, 245705.
22 Y. Lei, H. Song, L. Yang, L. Yu, Z. Liu, G. Pan, X. Bai and L. Fan, *J. Chem. Phys.*, 2005, **123**, 174710.

23 W.-N. Wang, W. Widiyastuti, T. Ogi, I. W. Lenggoro and K. Okuyama, *Chem. Mater.*, 2007, **19**, 1723–1730.
24 K. Y. Jung, C. H. Lee and Y. C. Kang, *Mater. Lett.*, 2005, **59**, 2451–2456.
25 L. S. Wang, Y. H. Zhou, Z. W. Quan and J. Lin, *Mater. Lett.*, 2005, **59**, 1130–1133.
26 G. H. Mhlongo, O. M. Ntwaeaborwa, H. C. Swart, R. E. Kroon, P. Solarz, W. Ryba-Romanowski and K. T. Hillie, *J. Phys. Chem. C*, 2011, **115**, 17625–17632.
27 B. Yan and X.-Q. Su, *Opt. Mater.*, 2007, **29**, 1866–1870.
28 I. Djerdj, G. Garnweitner, D. Sheng Su and M. Niederberger, *J. Solid State Chem.*, 2007, **180**, 2154–2165.
29 X. Wang and Y. Li, *Chem.–Eur. J.*, 2003, **9**, 5627–5635.
30 B. Tang, J. Ge, C. Wu, L. Zhuo, J. Niu, Z. Chen, Z. Shi and Y. Dong, *Nanotechnology*, 2004, **15**, 1273.
31 I. Kamińska, K. Fronc, B. Sikora, M. Mouawad, A. Siemiarczuk, M. Szewczyk, K. Sobczak, T. Wojciechowski, W. Zaleszczyk, R. Minikayev, W. Paszkowicz, P. Stępień, P. Dziawa, K. Ciszak, D. Piątkowski, S. Maćkowski, M. Kaliszewski, M. Włodarski, J. Młyńczak, K. Kopczyński, M. Łapiński and D. Elbaum, *RSC Adv.*, 2015, **5**, 78361–78373.
32 S. Zhao, W. Liu, X. Xue, Y. Yang, Z. Zhao, Y. Wang and B. Zhou, *RSC Adv.*, 2016, **6**, 81542–81551.
33 P. Ramasamy, P. Chandra, S. Woo Rhee and J. Kim, *Nanoscale*, 2013, **5**, 8711–8717.
34 P. Li, L. Guo, C. Liang, T. Li and P. Chen, *Mater. Sci. Eng. B*, 2018, **229**, 20–26.
35 N. Niu, F. He, S. Gai, C. Li, X. Zhang, S. Huang and P. Yang, *J. Mater. Chem.*, 2012, **22**, 21613–21623.
36 Y. Zhu, S. Zhao, B. Zhou, H. Zhu and Y. Wang, *J. Phys. Chem. C*, 2017, **121**, 18909–18916.
37 M. Ding, Y. Ni, Y. Song, X. Liu, T. Cui, D. Chen, Z. Ji, F. Xu, C. Lu and Z. Xu, *J. Alloys Compd.*, 2015, **623**, 42–48.
38 B. Zhou, B. Xu, H. He, Z. Gu, B. Tang, Y. Ma and T. Zhai, *Nanoscale*, 2018, **10**, 2834–2840.
39 S. Sinha, M. Kumar Mahata, H. C. Swart, A. Kumar and K. Kumar, *New J. Chem.*, 2017, **41**, 5362–5372.
40 P. Sudhakar, A. Siva Sesha Reddy, Ya. Zhydachevskyy, A. Suchocki, M. G. Brik, V. Ravi Kumar, M. Piasecki and N. Veeraiah, *Opt. Mater.*, 2018, **86**, 87–94.
41 S. K. Singh, K. Kumar and S. B. Rai, *Appl. Phys. B*, 2009, **94**, 165–173.
42 A. Rosencwaig and A. Gersho, *J. Appl. Phys.*, 2008, **47**, 64–69.
43 M. I. Sarkar, N. K. Mishra and K. Kumar, *Methods Appl. Fluoresc.*, 2022, **11**, 014002.
44 M. I. Sarkar and K. Kumar, *RSC Adv.*, 2023, **13**, 12723–12730.
45 V. Babin, P. Bohacek, L. Grigorjeva, M. Kučera, M. Nikl, S. Zazubovich and A. Zolotarjovs, *Opt. Mater.*, 2017, **66**, 48–58.
46 S. Sinha, A. Mondal, K. Kumar and H. C. Swart, *J. Alloys Compd.*, 2018, **747**, 455–464.
47 R. K. Tamrakar, D. P. Bisen, K. Upadhyay and I. P. Sahu, *J. Phys. Chem. C*, 2015, **119**, 21072–21086.
48 H. Liu, X. He, H. Jia, Y. Zheng, R. Bai and Y. Zhang, *Optik*, 2021, **228**, 166155.
49 G. Bilir and O. Erguzel, *Mater. Res. Express*, 2016, **3**, 106201.
50 S. Balabhadra, M. L. Debasu, C. D. S. Brites, R. A. S. Ferreira and L. D. Carlos, *Opt. Mater.*, 2018, **83**, 1–6.
51 K. Shwetabh, M. M. Upadhyay and K. Kumar, *RSC Adv.*, 2023, **13**, 9377–9386.
52 S. K. Singh, K. Kumar and S. B. Rai, *Mater. Sci. Eng. B*, 2010, **166**, 180–184.